Ultrafast lattice dynamics and electron-phonon coupling in laser-excited platinum

Daniela Zahn,[1, *] Hélène Seiler,[1] Yoav William Windsor,[1] and Ralph Ernstorfer[1, †]

[1] *Fritz-Haber-Institut der Max-Planck-Gesellschaft, Faradayweg 4-6, 14195 Berlin, Germany*

Platinum is an important component of heterostructures for novel photocatalysis and spintronic applications. Since these applications involve nonequilibrium states, knowledge of how platinum behaves in nonequilibrium conditions is desired. In particular, a quantitative determination of the electron-phonon coupling parameter G_{ep} of bulk platinum is of importance. Here, we study the lattice response of platinum to laser excitation directly using femtosecond electron diffraction. We provide details about our new approach for analyzing time-resolved polycrystalline diffraction data, which extracts the lattice dynamics reliably by finding the best fit to the full transient diffraction pattern rather than by analyzing transient changes of individual Debye-Scherrer rings. Based on the results for the transient evolution of atomic mean squared displacement (MSD) in platinum and using a two-temperature model (TTM), we extract $G_{ep} = (3.14 \pm 0.09) \cdot 10^{17} \frac{W}{m^3 K}$. We find that within our range of absorbed energy densities, G_{ep} is not fluence-dependent. Our results for the lattice dynamics of platinum provide insights into electron-phonon coupling and phonon thermalization and constitute a basis for quantitative descriptions of platinum-based heterostructures in nonequilibrium conditions.

I. INTRODUCTION

Platinum is important to many technological fields, and in particular it is often used as a catalyst. Many chemical reactions require high temperatures and/or pressures, rendering them energy-intensive. A promising approach to reduce this energy cost is to employ photocatalysis. One emerging approach is to employ bimetallic heterostructures that combine a catalytically active material (e.g. platinum or palladium) with a plasmonic material (e.g. silver, gold or aluminum)[1], for example in so-called antenna-reactor nanostructures[2,3]. It has been demonstrated that such structures can exhibit high photocatalytic activities[2,4]. In many photocatalytic reactions, highly excited ("hot") electrons play the decisive role[5–7]. The time scales on which the electrons remain hot depends on their coupling to other degrees of freedom, in particular the lattice, which is the main heat sink on ultrafast time scales. Therefore, knowledge about the ultrafast lattice dynamics is important for understanding the dynamics of hot-carrier driven chemical reactions.

In addition to its use in catalysis, platinum is also an important material for spintronics due to its large spin-orbit coupling. This leads for example to a large Spin-Hall effect, which is widely employed for spin-to-charge and charge-to-spin conversion[8–15]. The functionality of spintronic heterostructures is determined by the interplay of interfacial couplings and couplings within the individual materials. The relaxation processes within a material can therefore strongly influence charge and spin currents across interfaces. For example, the spin-Seebeck current across a photoexcited yttrium iron garnet/platinum interface strongly depends on the electronic temperature in platinum[16], whose evolution is dominated by electron-lattice equilibration. Therefore, knowledge of the lattice response of platinum serves as a basis for understanding and controlling the behavior of spintronic devices.

In particular, it is of interest to quantify the coupling of excited carriers to the lattice. However, literature values for the electron-phonon coupling constant G_{ep} of platinum vary significantly[7,17–20], from $2.5 \cdot 10^{17} \frac{W}{m^3 K}$[18] to $(10.9 \pm 0.5) \cdot 10^{17} \frac{W}{m^3 K}$[19]. So far, most values for G_{ep} in platinum were deduced using optical methods, for example time-resolved optical reflectivity (TRR) measurements[18–21]. A challenge of TRR measurements is that the reflectivity change depends on both the electron and the phonon temperatures[22–24], and separating these contributions is non-trivial. In addition, the dependence of the reflectivity change on these temperatures is not always linear, especially for higher fluences[25,26] and for transition metals[18]. An alternative way to access G_{ep} is by using a ferromagnetic detection layer in combination with time-resolved MOKE measurements[17]. However, this approach relies on modeling the nonequilibrium responses of both platinum as well as the detection layer, which limits the precision of the method. Apart from optical techniques, time-resolved photoemission also provides insights into the electron dynamics after laser excitation. The transient electron temperature evolution has been investigated with time-resolved photoemission, but only for few different time delays after photoexcitation[7]. Furthermore, in photoemission it can be difficult to separate population changes from changes of the band structure itself, and transport effects may influence the results due to the surface-sensitivity of the technique. Hence, time-resolved diffraction is an important complementary technique to optical and photoemission measurements. It is only sensitive to the lattice and can therefore directly measure the lattice response to photoexcitation, thus providing quantitative insights into electron-lattice equilibration from the lattice perspective.

Here we study the ultrafast lattice dynamics of laser-excited platinum using femtosecond electron diffraction. We fit the experimental results for the lattice heating to a two-temperature model[27,28] (TTM) and extract a

value for the electron-phonon coupling parameter. We also discuss the role of non-thermal phonons in the lattice dynamics. Our results provide quantitative information about electron-lattice equilibration as well as phonon thermalization, which are integral to the understanding of nonequilibrium dynamics in platinum.

II. EXPERIMENT

We study the lattice dynamics of platinum using the compact femtosecond electron diffractometer described in Ref.[29]. The sample is a freestanding, polycrystalline film of platinum with a thickness of 15 nm. It was deposited on a NaCl single crystal using electron beam evaporation. Then, the platinum film was transferred to a standard TEM grid using the floating technique[30]. To excite the sample, we use infrared laser pulses with a photon energy of 0.70 eV and a pulse length of around 80 fs (FWHM). The lattice response to photoexcitation is probed using ultrashort electron pulses with a kinetic energy of 70 keV. The estimated time resolution of the experiment is around 170 fs. The electrons are diffracted by the sample and diffraction patterns are recorded in transmission. Figure 1(a) shows a schematic illustration of the electron diffraction experiment, including a diffraction image of our platinum sample.

Since our sample is polycrystalline, we observe Debye-Scherrer rings. Therefore, we radially average the diffraction images for further analysis. The resulting radial average (RA) is displayed in Fig. 1(b). Our main observable is the intensity of the diffraction rings, which weaken as the atomic mean squared displacement (MSD) increases when additional phonons are created (Debye-Waller effect). The relationship between the intensity decrease and the MSD is given by[31]:

$$\frac{I(t)}{I_0} = \exp\{-\frac{1}{3} q^2 \Delta\langle u^2 \rangle(t)\} \tag{1}$$

Here, $\Delta\langle u^2 \rangle(t)$ is the MSD change, I_0 is the intensity before laser excitation and q is the scattering vector of the diffraction ring, $q = 4\pi \sin(\theta)/\lambda$.

III. GLOBAL DIFFRACTION DATA ANALYSIS

To analyze the time-resolved polycrystalline diffraction data, we utilize a fit routine in which the MSD is extracted using the whole RA, instead of specific Debye-Scherrer rings. A major advantage of this approach is that the total number of fit parameters can be reduced significantly, especially for the description of the laser-induced changes in the diffraction pattern. This is possible since some information is encoded in all diffraction rings, namely lattice expansion and MSD increase. Therefore, a global fit can increase the reliability of the results, by avoiding artifacts such as
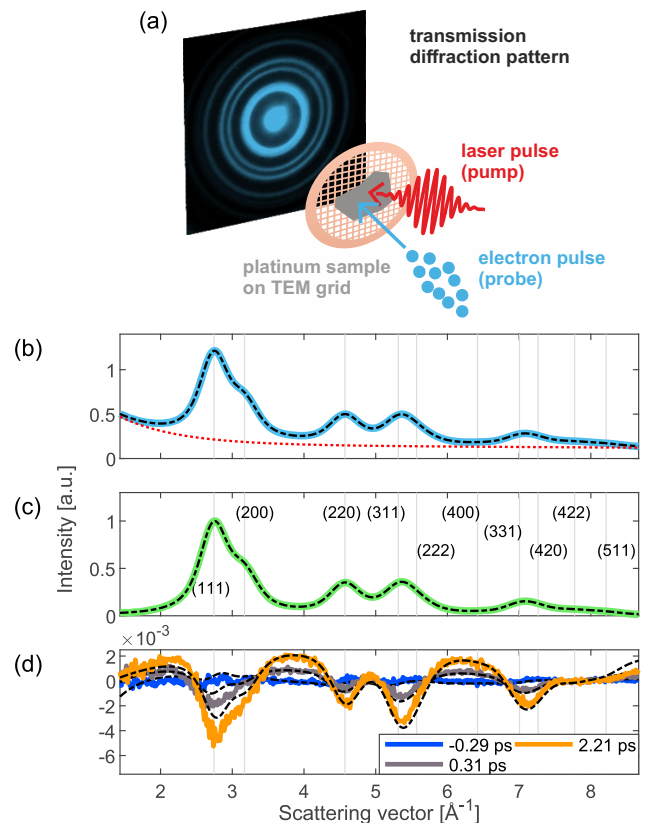

FIG. 1. Experimental setup and diffraction pattern of platinum. (a) Schematic illustration of the electron diffraction experiment. The freestanding thin-film sample is excited with an ultrashort laser pulse and the lattice response is probed with an ultrashort electron pulse. Diffraction patterns for several pump-probe delays are recorded in transmission. (b) Radially averaged diffraction pattern (RA) of our platinum sample. The solid blue line corresponds to the experimental data and the dashed black line represents the static global fit (see text for details about the fit). The dashed red line shows the static fit result for the background contribution. (c) Radially averaged diffraction pattern after subtracting the fit result for the background. The solid green line shows the experimental data and the dashed black line shows the static fit result without the background contribution. (d) Differences between the RA's for selected delays after photoexcitation and the RA prior to photoexcitation. The experimental data are shown as solid lines and the fit results of the dynamic fit are shown as dashed black lines. Note that in Panels (b)-(d), the x-axis was converted from image pixels to scattering vectors using the results of the static fit (for illustration purposes).

cross-talk of overlapping diffraction rings. Disentangling the dynamics of overlapping rings is particularly important in time-resolved electron diffraction due to the finite coherence of the pulsed electron sources. In the following, we provide more details about our global fit routine, which consists of two steps: In the first step (static fit), we perform a fit of the RA's before

laser excitation. In the second step (dynamic fit), a fit is performed to describe the changes of the RA's following laser excitation. Here, we only include changes due to an increase of the phonon population, hence we do not include any photo-induced rearrangement of atoms within the unit cell, e.g. structural phase transitions. The second step of our fitting routine yields the MSD change, the lattice expansion (i.e., the changes in diffraction ring radii) and the background change as a function of pump-probe delay.

A. Static fit

In the first step of the fitting routine, the goal is to accurately describe the RA's before laser excitation. For this step, first we average all RA's recorded before the arrival of the pump pulse in order to obtain maximum signal-to-noise ratio. For the fit, we use a wide range of reciprocal space that includes the first ten diffraction rings of platinum, from the (111) to the (511) reflection, as shown in Fig. 1(c).

Our fit function consists of the sum of a background function and peak functions for the radially averaged diffraction rings. The possibility of fitting all diffraction rings and a global background together in the same step is an additional advantage of the global fit, because it yields a reliable background determination. This becomes important in the second step of the fitting routine (dynamic fit), because the background subtraction strongly influences the results for the amplitude of the MSD increase.

The positions of the diffraction rings in reciprocal space are known. Thus, in order to reduce free parameters in the fit, we don't consider them as independent variables. However, in practice, our magnetic lens used to focus the electron beam on the detector can introduce image distortions, which cause a non-linear relationship between scattering vector and pixel number in the RA's. To account for these distortions, we introduce a correction parameter γ as a fit parameter. The radius of the first ring, r_1, is also a fit parameter and accounts for the conversion of scattering vectors to image pixels. The other ring radii are then given by:

$$r_i = \left(\frac{q_i}{q_1} \right)^{\gamma} \cdot r_1 \qquad (2)$$

Here, q_i are the scattering vectors of the diffraction rings. In our case, the magnetic lens introduces a barrel distortion, and therefore the fit result for γ is a value slightly smaller than one (here: around 0.96). We expect that our distortion correction can also correct pincushion distortions ($\gamma > 1$).

With Eq. 2, the approximate ring radii can be well described. In addition, to refine the ring radii, we introduced individual radius correction factors f_i as fit parameters. These were constrained such that the radii couldn't deviate more than 5% from the values

given by Eq. 2. We found that for our experimental data, introducing the individual correction factors f_i in addition to the global distortion correction γ is essential to obtain good agreement to the diffraction pattern before laser excitation, which then also determines the quality of the dynamic fit. However, note that most of the distortion is corrected by γ, which minimizes cross-talk of overlapping diffraction rings in the static fit. In the absence of distortions, or if distortions were corrected previously, the correction factors γ and f_i are not necessary and can be set to 1.

The radially averaged diffraction rings are described as Lorentzians with their amplitudes being unconstrained fit parameters. The width of the Lorentzians is one fit parameter (w_{reci}), such that the width of all rings in reciprocal space is the same. Due to the lens distortions, the widths in pixels, $w_i(w_{\mathrm{reci}}, r)$, are slightly different for the different rings. We don't consider broadening due to finite crystallite sizes according to the Scherrer equation, because the width of the rings is dominated by the finite coherence of the pulsed electron beam. In total, the function describing the diffraction rings is given by:

$$F(r) = \sum_{i=1}^{N} \frac{A_i}{\left(1 + \left(\frac{(r - r_i \cdot f_i)}{w_i} \right)^2 \right)} \qquad (3)$$

Here A_i are the amplitudes of the rings (fit parameters) and N is the number of diffraction rings considered. For the background function, we use a phenomenological function, which we choose depending on the experimental conditions. For the measurements presented here, we obtained the best agreement to the experimental data using an exponential function plus a linear relationship:

$$B(r) = a \cdot \exp\{-r/b\} + c + d \cdot r \qquad (4)$$

Here, we fixed b and d to a common value for all fluences.

Finally, the sum $F + B$ is convolved with a Gaussian to account for the finite coherence of the experiment. The convolution width is a fit parameter. Since there are also lens distortions which are not radially symmetric, the outer rings are typically slightly broader in the RA. To account for this, we introduce an additional fit parameter δ which distorts the radius axis linearly before the convolution:

$$r' = r \cdot (1 - \delta \cdot \frac{r - r_{\mathrm{start}}}{r_{\mathrm{end}} - r_{\mathrm{start}}}) \qquad (5)$$

r_{start} and r_{end} are the radii of the beginning and the end of the fit range, respectively. Note that this correction might not always be necessary, depending on the amount of distortions in the experimental data.

Finally, it should be noted that the width of the Lorentzians and the Gaussian broadening are strongly correlated and therefore the fit result depends on the starting values. Therefore, we varied these starting values and chose the optimal ones based on the residuals

of the fit. With this fitting procedure, we obtain excellent agreement to the experimentally measured diffraction pattern, as shown in Figure 1(b) and (c). The excellent agreement of the static fit to the experimental data is a very important prerequisite for the second step of the fitting routine, the dynamic fit.

B. Dynamic fit

In the second step, we analyze changes in the diffraction pattern following laser excitation. In this step, we make use of the results of the static fit, and only allow the following changes to the diffraction pattern compared to the static fit:

- decreases of the diffraction ring intensities corresponding to an MSD increase, according to Debye-Waller theory (see Eq. 1).

- expansion (or contraction) of the sample, leading to a reduction (increase) of the scattering vectors of all rings:

$$q_i(t) = q_{i,0} \cdot \left(\frac{1}{1 + \epsilon(t)} \right) \tag{6}$$

Here, $q_{i,0}$ is the scattering vector before laser excitation.

- changes of the background parameters. Following laser excitation, the background increases due to an increase in diffuse scattering.

Note that this description of the photo-induced changes of the diffraction ring intensities is valid for mono-atomic materials with one site symmetry. It can be extended to more complex materials, based on the crystal structure and the atomic form factors of the constituent materials.

Especially for low fluences, the noise level of the fit results can be significantly improved by constraining the background parameters, since often the parameters are correlated and local minima are possible. Here we restricted the change in background parameters to no more than a certain (fluence-dependent) percentage from one delay point to the next. Care was taken to ensure that the fit constraints do not alter the results for the lattice dynamics.

Figure 1(d) presents the differences of the RA's compared to the static RA for several pump-probe delays, as well as the fit results. We obtain good agreement to the experimentally observed changes. The deviations of the ring intensity changes are due to second-order scattering effects beyond the kinematic limit, which are not captured by Eq. 1. Second-order scattering is relatively strong in platinum due to its high atomic number and density. For transient MSD changes extracted from changes of individual diffraction rings, this effect leads to ambiguities because different rings yield different results. In contrast, the global fit

yields only one value for the MSD increase from all rings combined. Since second-order scattering increases the pump-probe effect of lower-order diffraction rings while decreasing the pump-probe effect of higher-order diffraction rings at the same time (compare Fig. 1(d)), we expect the global fit to yield relatively accurate results for the MSD even in the presence of second-order scattering.

In addition to the deviations caused by second-order scattering, there are deviations at both ends of the reciprocal space range considered for the analysis, which we attribute to the limitations of the phenomenological background function (see Eq. 4). However, for most of the range considered, both the background and the diffraction rings are well described by the result of the global fit.

IV. RESULTS AND DISCUSSION

The MSD evolution as a function of pump-probe delay is presented in Figure 2. We observe a two-
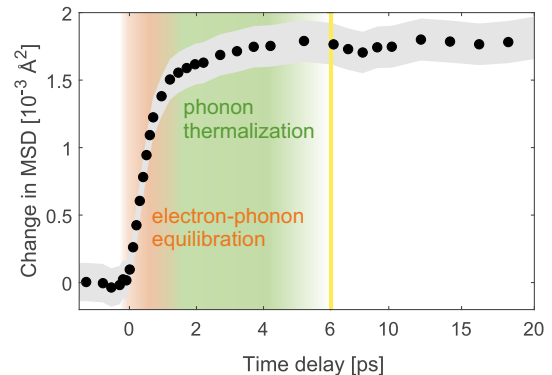

FIG. 2. Change of atomic mean squared displacement (MSD) as a function of pump-probe delay. The grey shaded area represents the error estimates of the data points, which correspond to the standard deviation obtained from the fitting routine. The yellow line indicates a change of scaling of the time axis. The absorbed energy density of this measurement was $102 \, \mathrm{J/cm^3}$.

step behavior: A fast component with a time constant of around 600 fs and slower, few-picosecond component with a much smaller amplitude. We attribute the fast component to electron-phonon equilibration and the slow component to phonon redistribution processes. Since the second component is a further MSD increase, these phonon redistribution processes correspond to energy transfer from higher to lower phonon frequencies, since lower-frequency modes exhibit higher displacements per phonon[31]. In addition, higher-frequency phonons decay into several low-frequency phonons due to their higher energy. Hence, we attribute the slow component of the lattice dynamics to a population increase of low-frequency phonon modes that couple relatively weakly to

the electrons and to other phonon modes. Nevertheless, in platinum, the amplitude of the second MSD rise is small compared to the initial MSD rise, which indicates that after the initial rise, most phonon modes have already thermalized with the electrons, except for a small subset of phonons.

In the following, in order to study electron-phonon coupling quantitatively, we focus on the initial, fast rise of the MSD, i.e. the time scale from -1 to 3 ps. We convert the MSD rise to lattice temperature using the temperature-dependent Debye-Waller factor provided by Ref.[31]. Based on the results for the lattice temperature, we employ a TTM to model the lattice heating and extract the electron-phonon coupling parameter G_{ep}. A schematic illustration of the TTM is displayed in Figure 3(a).

In the TTM, the material is described as consisting of two heat baths, electrons and phonons, which are always in internal thermal equilibrium. The evolution of the system is described by two coupled differential equations and is governed by the magnitude of G_{ep} as well as by the electronic and lattice heat capacities.

Here, we use the electronic heat capacity calculated by Lin et al.[32]. Since platinum is a transition metal, the relationship between electronic heat capacity and temperature is not linear, especially for high electronic temperatures. For electronic temperatures smaller than ca. 700 K, the heat capacity calculated by Lin et al. roughly corresponds to $c_e = \gamma \cdot T$ with $\gamma \approx 400\,\mathrm{J/(m^3 K^2)}$. This value is in agreement to experimental results for the heat capacity of platinum at room temperature, as discussed in Ref.[17]. Here, we don't assume a linear relationship for c_e and directly use the results provided by Lin et al.. For the lattice heat capacity, we use the high-temperature limit derived from equipartition, $24.943\,\frac{J}{\mathrm{mol}K}$ (corresponding to $2.744 \cdot 10^6\,\frac{J}{m^3 K}$)[33,34]. This is a valid approximation since the Debye temperature of platinum, 240 K[33], is well below room temperature.

In the TTM, the laser pulse is assumed to be of Gaussian shape with a FWHM of 80 fs. The absorbed energy density and the electron-phonon coupling parameter G_{ep} are obtained by finding the best fit of the experimentally measured lattice temperature to the lattice temperature predicted by the TTM. For this fit, the lattice temperature predicted by the TTM is convolved with a Gaussian with a FWHM of 150 fs to account for the estimated duration of the electron pulses. The arrival time of the laser pulse is the same for all fluences, because all measurements presented here were part of the same data acquisition. To obtain the most accurate value for the arrival time, we first performed TTM fits of the individual measurements with the arrival time as a fit parameter. Then, we calculated the weighted average of the resulting arrival times and repeated the TTM fits with the arrival time fixed at this value.

The evolution of the lattice and electronic temperatures resulting from the TTM fit are displayed in Figure 3(b)-(f) for different fluences, together with the experimental results. The TTM fit results are in excellent agreement with the experimentally measured lattice temperatures.

The TTM fit result values for G_{ep} are shown in Fig. 3(g). We don't observe any fluence dependence of G_{ep}. In principle, based on theoretical calculations, G_{ep} is expected to depend on the electronic temperature[32]. However, since the maximum electronic temperature in our experiments is only around 700 K, for our range of fluences a constant G_{ep} is a good approximation. We therefore calculate the weighted average of the G_{ep} results for different fluences. The result is $(3.14 \pm 0.09) \cdot 10^{17}\,\frac{W}{m^3 K}$. Figure 3(g) shows this value as a horizontal dashed line. Table I compares our result to existing literature values. Our result is within the range of previously measured values. However, note that most literature values for G_{ep} were extracted with the electron heat capacity coefficient from low-temperature measurements ($\gamma \approx 750\,\frac{W}{m^3 K^2}$). For transition metals like platinum, this is likely an imprecise assumption at room temperature, since their electronic density of states varies strongly around the Fermi level[32]. Since the time evolution of the temperatures in the TTM depends not only on the electron-phonon coupling, but also on the heat capacities, values for G_{ep} extracted with different γ-values are not directly comparable.

The large spread of literature values for G_{ep} (in particular also for similar γ-values) demonstrates that it is non-trivial to extract G_{ep} from time-resolved experimental data. Compared to measurements on heterostructures, our experiments have the advantage that the sample is much less complex and no transport effects between different layers occur. In addition, our sample is freestanding, hence there is no carrier and heat transport to a substrate either. Finally, our films are very thin and we probe in transmission, hence transport effects within the platinum layer can also be neglected. Therefore, the lattice response we measure reflects only the intrinsic, microscopic relaxation processes in platinum, which reduces the complexity of extracting G_{ep} from the data.

The extraction of G_{ep} with the TTM is based on the assumption that the two heat baths, electrons and phonons, are always in internal thermal equilibrium. For the electrons, particularly in metals, this is usually a good approximation, since electron-electron scattering is typically more efficient than electron-phonon coupling. For the phonons, a thermal distribution is not always a good approximation on short time scales after excitation[35–42]. Indeed, also for platinum, we observed signatures of phonon redistribution processes, indicated by the presence of a second, slow MSD rise, as discussed above. However, compared to the initial fast rise of the MSD, the amplitude of the second rise associated with phonon redistribution processes is rather small.
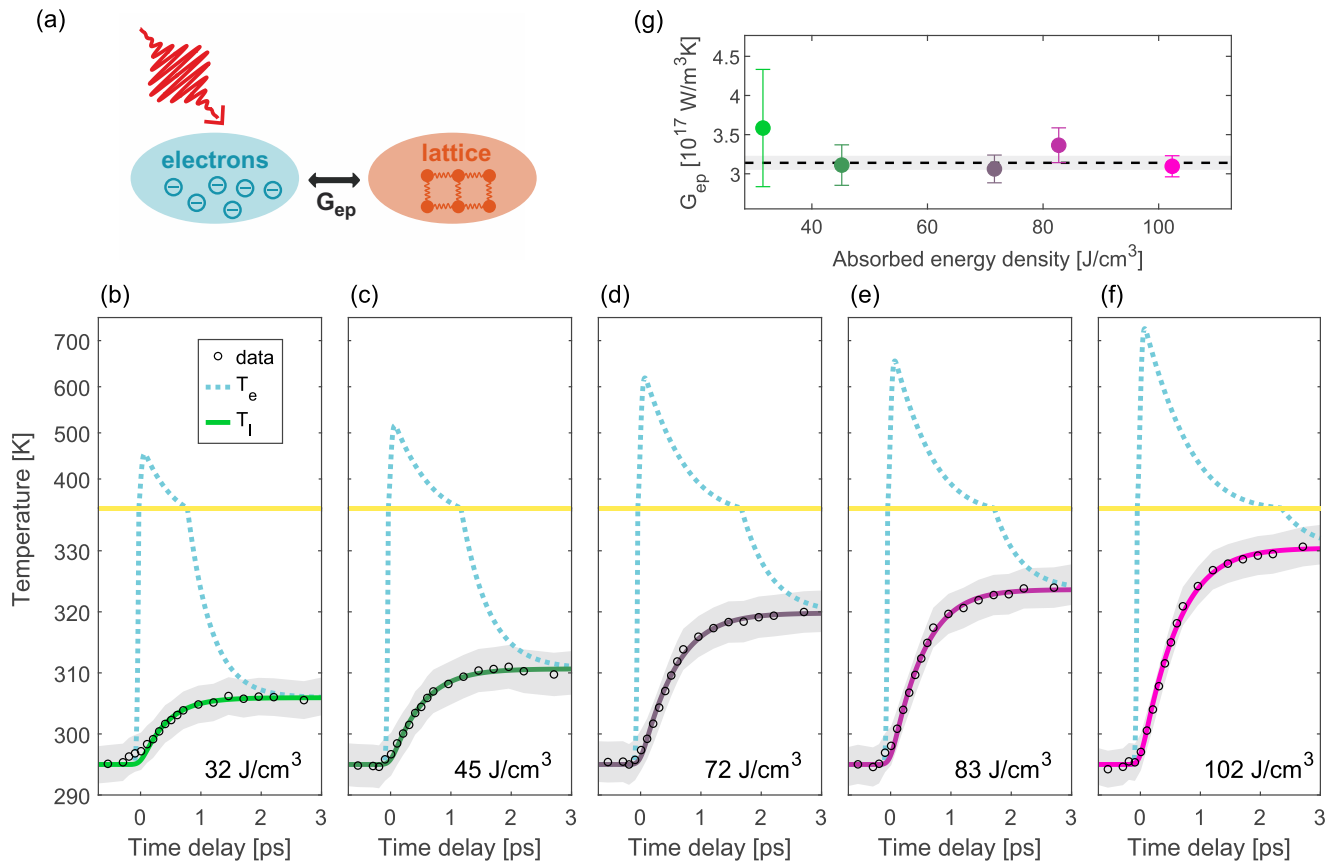
FIG. 3. Quantitiative determination of the electron-phonon coupling constant in platinum using a two-temperature model (TTM). (a) Schematic illustration of the TTM. (b)-(f) Experimental data together with temperature evolution according to the TTM fit result for different absorbed energy densities. The dashed blue lines correspond to the evolution of the electronic temperatures (T_e) and the green to pink lines display the evolution of the lattice temperatures (T_l). The experimental results for the lattice temperatures are displayed as black circles. The errors of the experimental data points are displayed as grey shaded areas and correspond to the standard error obtained from the fit of the RA's. (g) TTM fit result for the electron-phonon coupling parameter G_{ep} for the absorbed energy densities of Panels (b-f). The error bars for the G_{ep} values correspond to the standard error obtained from the TTM fit. The dashed black line corresponds to the weighted average of the G_{ep} values for different absorbed energy densities, and the grey shaded area represents the error of the weighted average.

This indicates that after the initial electron-phonon equilibration, the phonon population is already close to a thermal population. Hence, we conclude that for the purpose of describing energy flow from the electrons to the lattice, a TTM is a reasonable approximation.

V. SUMMARY AND CONCLUSIONS

In this work, we provide a direct measurement of the lattice dynamics of laser-excited platinum using femtosecond electron diffraction. We employ a global fitting routine to extract the changes of atomic mean squared displacement (MSD) reliably from the polycrystalline diffraction patterns, which we describe in detail. The MSD evolution exhibits two time scales: a sub-picosecond MSD rise, which we attribute to electron-phonon equilibration, and a further, much smaller MSD

rise on a few-picosecond time scale, which we attribute to phonon-phonon redistribution processes. Based on the dominant, fast MSD rise and using a two-temperature model (TTM), we extract a value of $(3.14 \pm 0.09) \cdot 10^{17} \frac{W}{m^3 K}$ for the electron-phonon coupling parameter G_{ep}. Within the range of fluences applied in our experiment, we don't observe any fluence dependence of G_{ep}. Compared to previous reports of G_{ep}, our approach has the advantage that our sample is a freestanding thin film, hence transport effects don't play a role in the dynamics. Furthermore, in contrast to optical spectroscopy, our technique is sensitive only to one subsystem, the lattice. We expect that a precise knowledge of the electron-phonon coupling in platinum will benefit the modeling and understanding of heterostructures containing this material, for example spintronic devices and photocatalytic structures.

Authors	G_{ep} [10^{17} J/(m^{3}K)]	Method	γ [J/(m^{3}K^2)]
Hohlfeld[18]	2.5	TRR	740
Kimling et al.[21]	2.9 ± 0.4	TRR (het.)	721
this work	**3.14 ± 0.09**	**tr-diffraction**	c_e from Lin et al.[32] ($\gamma \approx 400$)
Choi et al.[20]	4.2	TRR (het.)	721
Jang et al.[17]	6 ± 1	tr-MOKE (het.)	400
Lei et al.[7]	6.76	tr-photoemission	748
Caffrey et al.[19]	10.9 ± 0.5	TRR	750

TABLE I. Comparison of literature values for the electron-phonon coupling parameter G_{ep} of platinum. The third column lists the experimental method that was applied to obtain G_{ep}. Here, TRR stands for time-resolved reflectivity measurements, "tr" stands for time-resolved, MOKE corresponds to the magneto-optical Kerr effect and "(het.)" indicates that the data was recorded on a heterostructure. The last column lists the value for the electron heat capacity coefficient γ that was used to extract G_{ep}.

* zahn@fhi-berlin.mpg.de

† ernstorfer@fhi-berlin.mpg.de

[1] K. Sytwu, M. Vadai, and J. A. Dionne, Adv. Phys. X **4**, 1619480 (2019).

[2] L. Bai, X. Wang, S. Tang, Y. Kang, J. Wang, Y. Yu, Z.-K. Zhou, C. Ma, X. Zhang, J. Jiang, P. K. Chu, and X.-F. Yu, Adv. Mater. **30**, 1803641 (2018).

[3] C. Zhang, H. Zhao, L. Zhou, A. E. Schlather, L. Dong, M. J. McClain, D. F. Swearer, P. Nordlander, and N. J. Halas, Nano Lett. **16**, 6677 (2016).

[4] H. Robatjazi, J. L. Bao, M. Zhang, L. Zhou, P. Christopher, E. A. Carter, P. Nordlander, and N. J. Halas, Nat. Catal. **3**, 564 (2020).

[5] Y. Zhang, S. He, W. Guo, Y. Hu, J. Huang, J. R. Mulcahy, and W. D. Wei, Chem. Rev. **118**, 2927 (2018).

[6] L. Zhou, D. F. Swearer, C. Zhang, H. Robatjazi, H. Zhao, L. Henderson, L. Dong, P. Christopher, E. A. Carter, P. Nordlander, and N. J. Halas, Science **362**, 69 (2018).

[7] C. Lei, M. Bauer, K. Read, R. Tobey, Y. Liu, T. Popmintchev, M. M. Murnane, and H. C. Kapteyn, Phys. Rev. B **66**, 245420 (2002).

[8] K. Uchida, S. Takahashi, K. Harii, J. Ieda, W. Koshibae, K. Ando, S. Maekawa, and E. Saitoh, Nature **455**, 778 (2008).

[9] A. Kehlberger, U. Ritzmann, D. Hinzke, E.-J. Guo, J. Cramer, G. Jakob, M. C. Onbasli, D. H. Kim, C. A. Ross, M. B. Jungfleisch, B. Hillebrands, U. Nowak, and M. Kläui, Phys. Rev. Lett. **115**, 096602 (2015).

[10] I. M. Miron, K. Garello, G. Gaudin, P.-J. Zermatten, M. V. Costache, S. Auffret, S. Bandiera, B. Rodmacq, A. Schuhl, and P. Gambardella, Nature **476**, 189 (2011).

[11] I. Mihai Miron, G. Gaudin, S. Auffret, B. Rodmacq, A. Schuhl, S. Pizzini, J. Vogel, and P. Gambardella, Nat. Mater. **9**, 230 (2010).

[12] V. E. Demidov, S. Urazhdin, H. Ulrichs, V. Tiberkevich, A. Slavin, D. Baither, G. Schmitz, and S. O. Demokritov, Nat. Mater. **11**, 1028 (2012).

[13] T. Seifert, S. Jaiswal, U. Martens, J. Hannegan, L. Braun, P. Maldonado, F. Freimuth, A. Kronenberg, J. Henrizi, I. Radu, E. Beaurepaire, Y. Mokrousov, P. M. Oppeneer, M. Jourdan, G. Jakob, D. Turchinovich, L. M. Hayden, M. Wolf, M. Münzenberg, M. Kläui, and T. Kampfrath, Nat. Photon. **10**, 483 (2016).

[14] W. Yan, E. Sagasta, M. Ribeiro, Y. Niimi, L. E. Hueso, and F. Casanova, Nat. Commun. **8**, 661 (2017).

[15] T. Jungwirth, J. Wunderlich, and K. Olejník, Nat. Mater. **11**, 382 (2012).

[16] T. S. Seifert, S. Jaiswal, J. Barker, S. T. Weber, I. Razdolski, J. Cramer, O. Gueckstock, S. F. Maehrlein, L. Nadvornik, S. Watanabe, C. Ciccarelli, A. Melnikov, G. Jakob, M. Münzenberg, S. T. B. Goennenwein, G. Woltersdorf, B. Rethfeld, P. W. Brouwer, M. Wolf, M. Kläui, and T. Kampfrath, Nat. Commun. **9**, 2899 (2018).

[17] H. Jang, J. Kimling, and D. G. Cahill, Phys. Rev. B **101**, 064304 (2020).

[18] J. Hohlfeld, S.-S. Wellershoff, J. Güdde, U. Conrad, V. Jähnke, and E. Matthias, Chem. Phys. **251**, 237 (2000).

[19] A. P. Caffrey, P. E. Hopkins, J. M. Klopf, and P. M. Norris, Microscale Thermophys. Eng. **9**, 365 (2005).

[20] G.-M. Choi, C.-H. Moon, B.-C. Min, K.-J. Lee, and D. G. Cahill, Nat. Phys. **11**, 576 (2015).

[21] J. Kimling and D. G. Cahill, Phys. Rev. B **95**, 014402 (2017).

[22] R. Rosei and D. W. Lynch, Phys. Rev. B **5**, 3883 (1972).

[23] S. D. Brorson, A. Kazeroonian, J. S. Moodera, D. W. Face, T. K. Cheng, E. P. Ippen, M. S. Dresselhaus, and G. Dresselhaus, Phys. Rev. Lett. **64**, 2172 (1990).

[24] E. Carpene, E. Mancini, C. Dallera, M. Brenna, E. Puppin, and S. De Silvestri, Phys. Rev. B **78**, 174422 (2008).

[25] P. M. Norris, A. P. Caffrey, R. J. Stevens, J. M. Klopf, J. T. McLeskey, and A. N. Smith, Rev. Sci. Instrum. **74**, 400 (2003).

[26] A. N. Smith and P. M. Norris, Appl. Phys. Lett. **78**, 1240 (2001).

[27] S. I. Anisimov, B. L. Kapeliovich, and T. L. Perelman, J. Exp. Theor. Phys. **66**, 776 (1974).

[28] P. B. Allen, Phys. Rev. Lett. **59**, 1460 (1987).

[29] L. Waldecker, R. Bertoni, and R. Ernstorfer, J. Appl. Phys. **117**, 044903 (2015).

[30] J. R. Dwyer, R. E. Jordan, C. T. Hebeisen, M. Harb, R. Ernstorfer, T. Dartigalongue, and R. J. D. Miller, J. Mod. Opt. **54**, 923 (2007).

[31] L. Peng, S. Dudarev, and M. Whelan, *High Energy Electron Diffraction and Microscopy* (Oxford Science Publications, 2011).

[32] Z. Lin, L. V. Zhigilei, and V. Celli, Phys. Rev. B **77**, 075133 (2008).

[33] C. Kittel, *Introduction to solid state physics*, 8th ed. (Wiley, 2004).

[34] C. N. Singman, J. Chem. Educ. **61**, 137 (1984).

[35] L. Waldecker, R. Bertoni, H. Hübener, T. Brumme, T. Vasileiadis, D. Zahn, A. Rubio, and R. Ernstorfer, Phys. Rev. Lett. **119**, 036803 (2017).

[36] L. Waldecker, R. Bertoni, R. Ernstorfer, and J. Vorberger, Phys. Rev. X **6**, 021003 (2016).

[37] R. P. Chatelain, V. R. Morrison, B. L. M. Klarenaar, and B. J. Siwick, Phys. Rev. Lett. **113**, 235502 (2014).

[38] M. Trigo, J. Chen, V. H. Vishwanath, Y. M. Sheu, T. Graber, R. Henning, and D. A. Reis, Phys. Rev. B **82**, 235205 (2010).

[39] M. J. Stern, L. P. René de Cotret, M. R. Otto, R. P. Chatelain, J.-P. Boisvert, M. Sutton, and B. J. Siwick, Phys. Rev. B **97**, 165416 (2018).

[40] U. Ritzmann, P. M. Oppeneer, and P. Maldonado, arXiv:1911.12414.

[41] D. Zahn, P.-N. Hildebrandt, T. Vasileiadis, Y. W. Windsor, Y. Qi, H. Seiler, and R. Ernstorfer, Nano Lett. **20**, 3728 (2020).

[42] H. Seiler, D. Zahn, M. Zacharias, P. Hildebrandt, T. Vasileiadis, Y. W. Windsor, Y. Qi, C. Carbogno, C. Draxl, F. Caruso, and R. Ernstorfer, arXiv:2006.12873.